

Bar and berm dynamics during transition from dissipative to reflective beach profile

Florian Grossmann^{a,*}, David Hurther^b, Agustín Sánchez-Arcilla^a, Enrique M. Padilla^a, José M. Alsina^a

^a UPC BarcelonaTech, C. Jordi Girona, 1-3, Edifici D1, Barcelona, 08034, Spain

^b Laboratory of Geophysical and Industrial Flows (LEGI), CNRS, Grenoble INP, Université Grenoble Alpes, Grenoble, France

ARTICLE INFO

Keywords:

Sandbar
Beach face
Surf-swash sand exchange
Wave breaking
Berm overwash

ABSTRACT

Bar and berm morphology characterize the seasonal beach evolution, and determine the protection against storm erosion as well as the touristic use of beaches. Thus, they are of particular interest for coastal management and engineering in the nearshore zone. This study used large-scale wave flume experiments to observe the transition from fully dissipative to fully reflective beach profile at a high level of detail. Starting from a post-storm profile generated under energetic waves, a very low energy wave condition caused dissipation of the outer and the inner bar, shoreline recovery, and berm accretion. Measurements revealed feedback between hydrodynamics and beach profile evolution with an onshore shift of the wave breaking location. As a result, the magnitude and cross-shore evolution of wave asymmetry-related bedload net onshore and suspended net offshore transport changed. The relative magnitudes of the two transport components and the way they shifted relative to each other caused the observed beach recovery. Additionally, a link between bar and berm morphology (surf-swash sand exchange) was observed. The shifting breakpoint enabled sustained, wave asymmetry-related onshore transport in the inner surf zone, feeding the berm accretion which occurred through advective swash zone processes including berm overwash.

1. Introduction

It is well-known that sandy beaches around the world cycle through seasonal states (Winant et al., 1975; Wright and Short, 1984). Energetic wave conditions, typically occurring in winter, erode sediment from the shoreline and deposit it in one or multiple offshore-migrating sand bars. The bars promote wave breaking so that incoming wave energy is dissipated over a large cross-shore extent. Therefore, such beach profiles are referred to as “dissipative profiles”. Under less energetic conditions, typically occurring in summer, sediment is transported back to the shoreline, so-called beach recovery. This occurs either through bar maintenance during onshore migration or bar dissipation (Eichentopf et al., 2018; Grossmann et al., 2023b). As a result, the shoreline steepens and berms grow (accrete). The steep profiles typically enhance the reflection of incoming wave energy. Therefore, they are termed “reflective profiles”.

In this context, sandbars are characteristic elements of the morphological evolution of beaches. They are defined as alongshore ridges on the seabed, typically located in the shoaling and surf zones of many beaches around the world (King and Williams, 1949; Wright and Short, 1984; Wijnberg and Kroon, 2002). Long-term field observations have

provided information on their yearly and decadal migration cycles (Wijnberg and Kroon, 2002; van Enckevort and Ruessink, 2003; Phillips et al., 2017; Ruiz de Alegría-Arzaburu and Vidal-Ruiz, 2018; Eichentopf et al., 2020b). However, due to limitations in temporal and spatial resolution, knowledge gaps on the processes of their formation, maintenance and migration remain. Especially under low energy conditions, morphological evolution is complex and detailed knowledge on processes is sparse (Eichentopf et al., 2018). This contributes importantly to the difficulties with long-term morphological simulation and the calibration dependency of models (Hsu et al., 2006; van Rijn et al., 2011; Dubarbier et al., 2015; Rafati et al., 2021).

Berms take an equally important role in characterizing the morphological evolution of beaches. They are defined as alongshore bodies of sediment with a slightly landward dipping top section and a more steeply dipping seaward slope, the beachface (Hine, 1979; Hughes and Turner, 1999; Jensen et al., 2009). Being located just landward of the shoreline, parts of the berm are momentarily submerged as waves propagate up the beachface. Therefore, they contribute sediment for aeolian transport and dune growth. Furthermore, they serve as a buffer for storm erosion and provide space for recreational beach use.

* Corresponding author.

E-mail address: florian.grossmann@upc.edu (F. Grossmann).

Table 1

Wave sequences in RESIST. A3 (accretive) sequence for detailed analysis herein marked in gray. Benchmark (B) random waves homogenized and compacted the manually shaped profile before start of the actual experiments.

Sequence	Test number	Wave condition	Duration [min]	Ω [-]
1	16	B	30	2.21
	17–23	E1	240	3.34
	24–35	A1	360	1.44
	36–39	E2	120	2.54
	40–51	A1	600	1.44
2	52	B	30	2.21
	53–56	E2	120	2.54
	57–68	A1	600	1.44
	69–74	E1	240	3.34
	75–86	A1	360	1.44
3	87	B	30	2.21
	88–91	E1	240	3.34
	92–104	A2	780	1.05
	105–108	E2	120	2.54
	109–132	A3	1440	0.72

Nevertheless, few studies have investigated the details of their formation and growth. Initially, [Hine \(1979\)](#) observed the complexity of multiple modes of berm formation. Additional field studies by [Weir et al. \(2006\)](#) and [Jensen et al. \(2009\)](#) added some information on the underlying processes. Controlled laboratory conditions allowed ([Ruessink et al., 2016](#)) to observe some of the processes in more detail. They stressed the importance of surf-swash sand exchange. In fact, the link between bar and berm morphology is of central importance for long-term morphological evolution ([Alsina et al., 2012](#)) and simulation ([Larson et al., 2016](#)), but large knowledge gaps remain ([Ruessink et al., 2016](#)).

This partly results from the complexity of the associated sediment transport processes. While a range of processes is known (for example, undertow [Gallagher et al., 1998](#) or wave asymmetry [Dibajnia and Watanabe, 1992](#)), the feedback with morphological evolution and the implications for sediment transport are difficult to quantify. In low energy beach recovery conditions this is exacerbated by the little data available. Thus, it remains difficult to simulate how sediments are transported from bars to the berm. In this context, recent field studies have observed increased beach recovery and berm accretion when bars migrated onshore close to the shoreline ([Phillips et al., 2017](#); [Ruiz de Alegría-Arzaburu and Vidal-Ruiz, 2018](#)). However, it was not clear how the bars affected processes at the berms and whether feedback processes played an important role.

The present study conducted large-scale wave flume experiments to provide novel insights on this. To do so, the transition from dissipative to reflective beach profile was replicated in controlled laboratory conditions. At the same time, sediment transport and its forcing conditions were measured. To provide more detail than many existing datasets, the experiments captured the whole cycle from post-storm, dissipative beach profile to a reflective beach profile in 24 h of experimentation time. Furthermore, they featured a high spatial and temporal resolution of measurements, including bedload sediment transport. The paper is organized as follows: Section 2 introduces the experimental setup and data treatment. Section 3 summarizes results on morphological evolution, hydrodynamic quantities and sediment transport. Furthermore, it provides details on specific aspects of morphological evolution such as bar dissipation and berm growth. Subsequently, the results are discussed and put into context with similar studies (Section 4) to form conclusions (Section 5).

2. Experimental setup and data analysis

The present data were acquired within the HYDRALAB+ transnational access project “Influence of storm sequencing and beach recovery on sediment transport and beach resilience” (RESIST). Details of

the experimental protocol and data analysis were already presented in [Eichentopf et al. \(2020a\)](#) and [Grossmann et al. \(2022\)](#), and only the most important aspects will be repeated here.

2.1. Facility and test conditions

The experiments were conducted in the large-scale CIEM wave flume at the Universitat Politècnica de Catalunya (UPC) in Barcelona. The flume is 100 m long, 3 m wide and 4.5 m deep, and it is equipped with a wedge-type wave paddle. The cross-shore coordinate x was defined as 0 at the wave paddle, increasing towards the beach. The absolute vertical coordinate z refers to the still water level (SWL; equaling 2.5 m in the present experiments) while the bed-referenced coordinate ζ' refers to the seabed and point upwards. For more details on the vertical reference systems see [Grossmann et al. \(2022\)](#). The flume contained medium-grained sand with a median sediment diameter (D_{50}) of 0.25 mm ($D_{10} = 0.154$ mm and $D_{90} = 0.372$ mm) and a measured still water settling velocity w_s of 0.034 m/s.

Bichromatic erosive (E1 and E2) and accretive (A1, A2 and A3) wave groups were applied in three different sequences ([Table 1](#)). Note that bichromatic waves allow clear separation of processes at different frequency bands ([Grossmann et al., 2023b](#)) while producing morphological evolution similar to random waves ([Baldock et al., 2011](#)). The present wave conditions are termed erosive and accretive because of their different dimensionless sediment fall velocities ($\Omega_{rms} = \frac{H_{rms}}{T_p \cdot w_s}$ with H_{rms} calculated from spectra measured at 20 m from the wave paddle). The present paper focuses on accretive condition A3 ($\Omega_{rms} = 0.72$, $H_{rms} = 0.14$, and $T_p = 5.7$) with primary frequency components $f_1 = 0.1877$ Hz and $f_2 = 0.1632$ Hz. Its wave group period (T_g) is defined as $T_g = \frac{1}{f_1 - f_2} = 40.85$ s and there were 7 short waves per group. The waves were characterized by a primary mean period of $T_p = \frac{1}{f_p} = 5.7$ s where $f_p = \frac{f_1 + f_2}{2}$. To assess the potential influence from basin seiching without active wave absorption (e.g., [Flick and Guza \(1980\)](#)), a wave separation technique ([Padilla and Alsina, 2020](#)) was applied, and influence from spurious energy was found to be negligible (see [Appendix](#)). The repetition period (T_r), i.e., the period after which a wave phase repeated exactly, contained three slightly differing, alternating wave groups so that $T_r = 3 \cdot T_g = 122.55$ s. In this study, T_r was of central importance because it determined the exact repetition for the ensemble-averaging procedure. The erosive condition (E2) which generated the post-storm profile that the accretive sequence start from, was characterized by $T_r = 29.58$ s, $\Omega_{rms} = 2.54$, $H_{rms} = 0.32$, and $T_p = 3.7$ (see [Grossmann et al. \(2022\)](#) for more information).

2.2. Instrumentation

Measurements were taken from a mobile frame which was repositioned horizontally at intervals to measure in various locations surrounding the migrating sandbars. The Acoustic Concentration and Velocity Profiler (ACVP; [Hurther et al. \(2011\)](#)) measured sediment concentrations, velocities and instantaneous bed elevations. It provided co-located sediment concentration and velocity measurements (cross-shore and vertical) as vertical profiles (1.5 mm bin size) of up to 20 cm above the bed. Additional concentration measurements inside the ACVP measuring domain were obtained from a three-nozzle Transverse Suction System (TSS) on the mobile frame (used for measurement validation as described in [Grossmann et al. \(2022\)](#)). Above the ACVP measuring domain, two Optical Backscatter Sensors (OBSs) were used to measure sediment concentrations at 40 Hz. Pointwise outer flow velocities (i.e., higher than 10 cm from the bed) were measured at 100 Hz using a vertical array of three Nortek Vectrino Acoustic Doppler Velocimeters (ADV). The lowermost ADV was located within the ACVP measuring domain, approximately 10–15 cm above the seabed. The other two mobile frame ADVs were located approximately 20–25 cm and 30–35 cm above the seabed respectively.

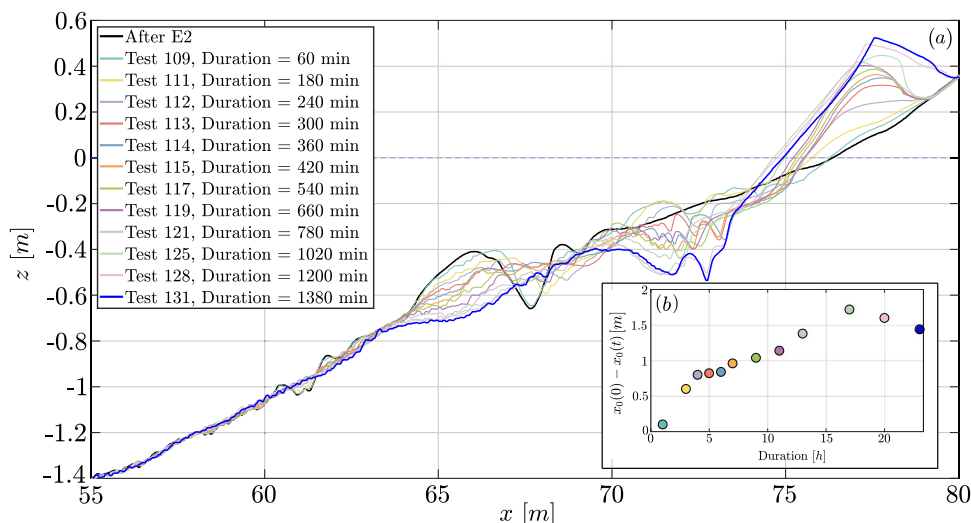


Fig. 1. Morphological evolution (a) and shoreline evolution (b) during tests with wave condition A3. SWL (dashed blue line) and beach profiles (solid lines) with cumulative time after the start of A3. Y-axis indicates distance from SWL and x-axis distance from the wave paddle. Inserted plot uses same colors (filled circle markers) to show corresponding evolution of the shoreline. Selection of tests to improve visibility.

Additional ADVs and OBSs were attached to the flume side-wall (far enough to not be affected by it) in the inner surf and swash zones. At times, those sensors were re-positioned horizontally to continue measuring in the lower swash zone as the beach profile evolved. Furthermore, their vertical elevation above the evolving bed was verified before each test and, if necessary, adjusted to be always at 3 cm above the bed. Water surface elevations were measured at 40 Hz using Resistive (wire) Wave Gauges (RWGs), Acoustic Wave Gauges (AWGs) and Pressure Transducers (PTs; conversion from pressure to water surface elevation following Bonneton et al. (2018)) in fixed locations along the flume. Active beach profile transects were measured in intervals of 60 min with a mechanical profiler, separating the A3 sequence into tests (numbered 109–132). The profile measurements were conducted along the centerline of the flume with a cross-shore resolution of 0.02 m and a vertical measuring accuracy of 0.01 m.

2.3. Data treatment

The same data cleaning and averaging procedures as explained in Grossmann et al. (2022) were applied. Net sediment transport rates were calculated from beach profile transect measurements using a mass balance equation (e.g., Baldock et al. (2011)) with porosity equal to 0.36. The ACVP, measuring from the mobile frame (Section 2.2), supplied profiles of sediment concentration following the methodology of Hurther et al. (2011). This is done by iterating downwards from the emitter while accounting for the signal attenuation due to sand grain scattering and water absorption occurring along the acoustic path, as described in detail by Fromant et al. (2018). This requires a single calibration constant which was equal in all the present tests and equal to previous analyses of RESIST data (Grossmann et al., 2023b). At times, the ACVP measured in the vicinity of the breakpoint where wave breaking-induced air bubbles may affect the signal (see Grossmann et al. (2022)). Thus, every ensemble of acoustic backscatter was subjected to visual inspection and spurious ensembles affected by air entrainment were removed. Only then, data were ensemble-averaged (at T_r , see Section 2.1) for in-depth analysis and representation in figures. The remaining ensembles still ensured a well-supported representation of near-bed sediment concentration and flow velocity in each test.

Fixed sensor measurements of water surface elevation, fluid velocity and sediment concentration were also ensemble-averaged. They were observed to be free from the signal attenuation problems described above. However, measurements in the swash zone are subject

to additional difficulties (for example sensor emergence) and require additional data cleaning procedures. First, ADV and OBS sensors were compared to the water surface elevation sensor horizontally closest to them (always within 7 cm). Their time-dependent measurements were only accepted if a minimum of 3 cm of water depth was present (so that the sensors were submerged). Second, OBS sensors get saturated at high suspended concentrations ($\geq 100 \text{ kg/m}^3$) and when they are buried by an evolving beach profile. Measurement ensembles were only accepted if less than 10% of T_r featured concentrations close to saturation. As a result of the two cleaning conditions, up to 9 out of 25 ensembles were rejected in certain tests. Nevertheless, the ensemble-averaged based on more than 15 ensembles is still considered representative.

3. Results

3.1. Morphological evolution

The sequence of A3 tests for detailed analysis in this paper (tests 109–132, see Table 1) started from a post-storm profile generated by erosive wave condition E2 (Fig. 1a; black line). This profile was characterized by outer and inner breaker bars. After the change to accretive wave condition A3, dissipation of the outer bar ($64 \leq x \leq 67 \text{ m}$) and erosion of the inner surf zone become visible ($69 \leq x \leq 74 \text{ m}$). Furthermore, a new inner bar is formed closer to the shoreline ($69 \leq x \leq 71 \text{ m}$) and a considerable berm is constructed ($76 \leq x \leq 80 \text{ m}$). In most of the tests, the shoreline ($x_0(t)$) progrades (Fig. 1b). Only towards the end (tests 128 or 131) the shoreline slightly retreats as the emerged beach steepens, completing the evolution from dissipative to reflective profile. The morphological evolution will be contextualized with its sediment transport (Section 3.2) and hydrodynamic conditions (Section 3.3). Key aspects of the morphological evolution will then be explained in detail and related to their sediment transport processes in Section 3.4.

3.2. Morphological evolution and sediment transport

Fig. 2 groups the tests into phases according to similarity of cross-shore transport (dashed lines and solid, dark blue line referring to right y-axis) calculated from a mass balance (Section 2.3 for details). Note that the figure shows data in relative x-coordinates, $x' = x - x_0(t)$, referenced with the shoreline position of each test. This is a commonly-used referencing method which makes key aspects more clearly visible and tests with morphologically-evolving beach profiles more easily comparable.

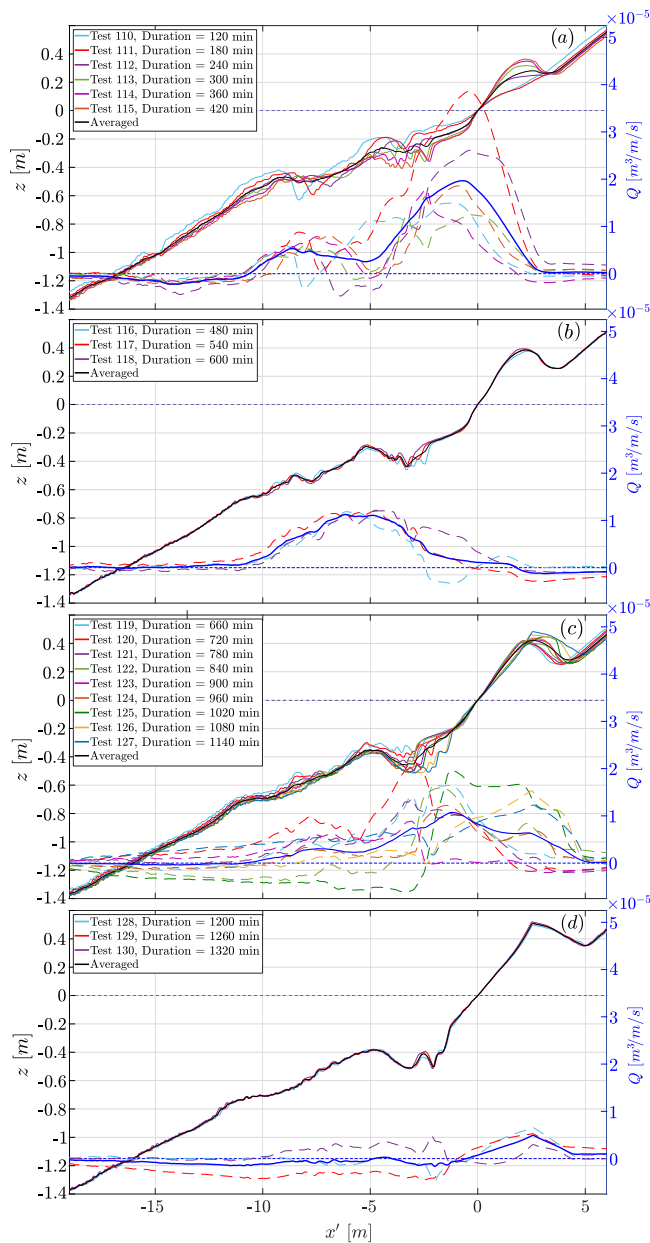


Fig. 2. Morphological phases (a–d) during tests with wave condition A3. SWL (dashed, transparent blue line) and beach profiles (solid lines; black lines showing test-averaged profiles) referring to left y-axis (distance from SWL). Net sediment transport (dashed lines; dark blue solid line showing test-averaged transport) calculated from mass balance referring to right y-axis. Data shown in relative x-coordinates, referenced with the shoreline position in each test.

The figure shows that net sediment transport is mostly onshore-directed. During the first 420 min of experimentation time (Fig. 2a), the largest transport magnitudes and cross-shore gradients (dQ/dx') are observed close to the shoreline. As a result, there is erosion in the inner surf zone ($-5 \leq x' \leq 0$ m) with sediment moving onshoreward to the emerged beach, constructing a berm ($0 \leq x' \leq 3$ m). Farther offshore, the gradients cause erosion of the outer bar's offshore slope ($-11 \leq x' \leq -9$ m) and filling of its trough ($-9 \leq x' \leq -7$ m). Note that largest transport magnitudes and gradients are observed in the tests coinciding with an onshore breakpoint shift (Section 3.3).

In the following tests (Fig. 2b), the largest transport magnitudes and gradients are observed at the bars. A single onshore transport maximum is visible, in contrast to the two maxima that were observed

previously. This causes erosion over the outer bar ($-10 \leq x' \leq -6$ m), and accretion of the inner bar ($-6 \leq x' \leq -4$ m) and inner surf zone ($-4 \leq x' \leq -2$ m). Compared to the previous phase (Fig. 2a), the magnitude of morphological evolution in each test is low, apart from a narrow extent of the inner surf zone ($-3 \leq x' \leq -2$ m).

Subsequently (Fig. 2c), the largest transport magnitudes and gradients are observed farther onshore once again. When comparing to Fig. 2a, erosion occurs over a narrower extent of the inner surf zone ($-5 \leq x' \leq -1$ m), resulting in a clearly-shaped inner bar, and the remnants of the outer bar are flattened out ($-9.5 \leq x' \leq -7.5$ m). At the same time, considerable accretion occurs at the berm ($0.5 \leq x' \leq 4.5$ m). Previously (Fig. 2a), berm accretion focused on the seaward slope, but now it focuses on the back berm, probably due to berm overwash (e.g., Baldock et al. (2005)). In the last tests (Fig. 2d), transport magnitudes and gradients are very low, and the beach profile changes little. In fact, during the A3 sequence there is a tendency towards less morphological evolution in subsequent tests, and at the end of the sequence the profile seems in quasi-equilibrium with the hydrodynamic forcing (see also Eichtopf et al. (2020a)).

The observed morphological evolution is summarized in the following phases:

- $t \leq 7$ h: Bar dissipation and initial berm growth
- $8 \text{ h} \leq t \leq 10$ h: Breaker bar reshaping
- $11 \leq t \leq 19$ h: Inner surf zone erosion and back berm growth
- $t \geq 20$ h: Quasi-steady hydro-morphological state

3.3. Morphological evolution and hydrodynamics

During all A3 tests the same wave realization was generated by the wave paddle. Nevertheless, as the beach profile evolved, interesting differences in nearshore wave propagation and wave breaking became visible. Fig. 3 contextualizes this by showing beach profiles (solid lines referring to left y-axis) with wave propagation (circle markers; AWG and RWG measurements) and breaking (dark blue lines referring to right y-axis) in the previously-identified four morphological phases (Section 3.2).

Initially, waves are observed to break at 3–5 m offshore of the shoreline (Fig. 3a, $-5 \leq x' \leq -3$ m). This is visible in H_{rms}/d clearly exceeding a commonly-used limit taken at 0.8 (horizontal, dark blue line; note that d excluded set-up/set-down which amounted to less than 2 cm over the barred region). The waves partially break at the outer bar (visual observations confirmed by a local maximum at $x' \approx -8$ m in Fig. 3a) but note that wave breaking in bichromatic wave groups is a gradual process with largest waves within the group breaking at larger water depth and smallest waves breaking closer to the shoreline (e.g., Padilla and Alsina (2017)), further discussed in Section 4. As a result of wave breaking the waves reach the shoreline as propagating bores, having dissipated some of their energy. Furthermore, wave propagation and breaking lead to erosion across the surf zone.

The larger water depth in the nearshore ($-15 \leq x' \leq 0$ m), in turn, leads to an onshore shift of breaking (Fig. 3b/c). This was observed in water surface elevation measurements along the wave flume (not shown for brevity) which show that the largest waves in the group pass the outer bar without a reduction in wave height. In fact, the onset of shoaling (a sign of depth interaction) was also observed to shift onshore. As a result, H_s/h decreases in general but especially at its maxima ($-8 \leq x' \leq -7$ m and $-6 \leq x' \leq -3$ m). In a feedback with small morphological changes, these shifts continue until (Fig. 3c) the commonly-used depth-induced breaking limit is not exceeded anymore (Test 121 onwards). While there may still be partial breaking during propagation over the bars, the focus of wave breaking clearly shifts towards the shoreline. As a result, bore propagation (and energy dissipation) occur over a smaller cross-shore extent so that more wave energy reaches the shoreline. This is confirmed by wave height measurements (discussed further in Section 3.4.3).

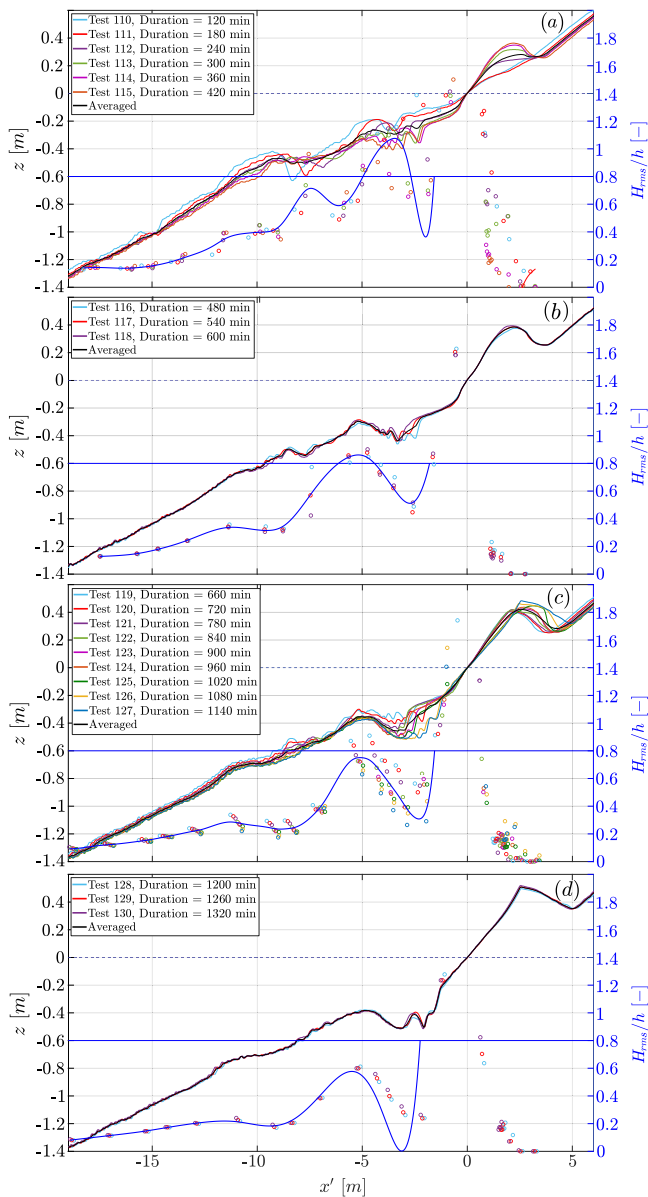


Fig. 3. Wave breaking during morphological phases (a–d) in tests with wave condition A3. SWL (dashed blue line) and beach profiles (solid lines; black lines showing test-averaged profiles) referring to left y-axis (distance from SWL). Depth-induced breaking limit (horizontal dark blue line), wave height over water depth measurements (circle markers), and smoothing spline interpolation (over all tests) of the measurements (dark blue line) referring to right y-axis. Data shown in relative x-coordinates, referenced with the shoreline position in each test.

In the meantime, the inner bar ($-6 \leq x' \leq -4.5$ m) erodes slowly in conjunction with most locations of the active submerged profile, especially the inner surf zone ($-3 \leq x' \leq -1$ m). Furthermore, the berm accretes considerably ($2.5 \leq x' \leq 5$ m). At the end of the sequence (Fig. 3d), hydrodynamics and beach profile are in equilibrium. This coincided with bore collapsing at the shoreline (visually observed).

3.4. Key aspects of morphological evolution and underlying processes

3.4.1. Outer bar dissipation

In the first A3 tests (tests 109–113), onshore migration and dissipation of the outer bar became visible (Figs. 1a/2a). At the same time, the outer bar trough was filled (completed in test 113). To provide more detail on this, Fig. 4 shows depth-integrated (total) sediment transport

measurements from the ACVP (Section 2.3) comparing the offshore (blue) and onshore (red) side of the bar.

In both locations, sediment transport under wave troughs (negative) is lower than the transport under crests (positive), causing the net onshore transport already observed from the mass balance (Fig. 2a). Furthermore, transport under troughs at the two locations is similar. Under the crests, however, the offshore side (blue) transports considerably more sediment onshore than the onshore side (red). This causes a larger net onshore transport (compare dashed, horizontal lines) on the offshore side. As a result, the cross-shore transport gradient over the outer bar is decreasing and accretion occurs. The outer bar trough is filled with sediment which, most likely, originated from the offshore slope of the outer bar.

After trough filling, the outer bar keeps eroding while the area between the bars slightly accretes (Figs. 1a/2a; tests 113–116). To provide more detail on this, Fig. 5 shows depth-resolved, time-averaged sediment flux measurements. Note that, to improve visibility of the fluxes, only a test-averaged beach profile (by averaging tests 113–116 in the x' -coordinate system) is shown.

When comparing tests offshore of the outer bar (115 and 116) to the tests onshore (113 and 114), the onshore tests show increased net onshore flux magnitude near the bed. In fact, most transport occurs as bedload within 1–2 cm of the bed and no considerable suspended transport is visible. The increased bedload causes continued erosion of the outer bar, supplying sediment to locations farther onshore.

3.4.2. Inner bar dissipation

Initially, the breakpoint was located at the inner bar (Fig. 3a). Commonly, wave breaking close to bars has been associated with their maintenance (for example Grossmann et al. (2023b)). Nevertheless, the present experiments featured dissipation of the inner bar, associated with an increasing cross-shore transport gradient (Fig. 2a) and followed by an onshore shift of the breakpoint (Fig. 3). To provide more detail on this, Fig. 6 shows ADV measurements of horizontal velocity and OBS measurements of sediment concentration at various cross-shore locations during dissipation of the inner bar (tests 111–113).

Fig. 6a/b shows that, at the inner bar, waves are skewed and asymmetric, and partially breaking. The waves generate low, offshore-directed undertow \bar{U} (dashed, horizontal lines). With decreasing breaking intensity over the inner bar (test 111 compared to 113 in Fig. 3a), undertow magnitude also decreases. At the same time, the waves generate considerable root-mean-squared velocity U_{rms} (dotted, horizontal lines). Furthermore, with decreasing breaking intensity over the inner bar (test 111 compared to 113), U_{rms} on the bar crest (a) decreases but increases in the bar trough (b). Moreover, little sediment suspension is observed at the bar trough (Fig. 6c) and offshore of it (not shown for brevity). Only close to the shoreline (Fig. 6d), sediment suspension considerably increases — even more so, as the breakpoint shifts onshore (compare tests 113 and 111).

Wave asymmetry has often been associated with net onshore transport, especially in relation to bedload (for example Grossmann et al. (2023b)). Similarly, U_{rms} has been associated with net onshore transport (e.g., Rafati et al. (2021)). Thus, the velocity measurements indicate a continued, or even increasing, net onshore transport from bar crest (Fig. 6a) to bar trough (Fig. 6b). At the same time, sediment suspension and undertow were low around the bar (Fig. 6). They usually cause the suspended net offshore transport required for bar maintenance (Grossmann et al., 2023a). Consequently, it seems likely that low suspended net offshore transport could not balance increasing bedload net onshore transport, resulting in increasing net onshore transport and erosion. The inner bar dissipates and supplies sediment to the shoreline, and, especially after the breakpoint shift, to berm growth (Fig. 1a; $x \leq 74.5$ m).

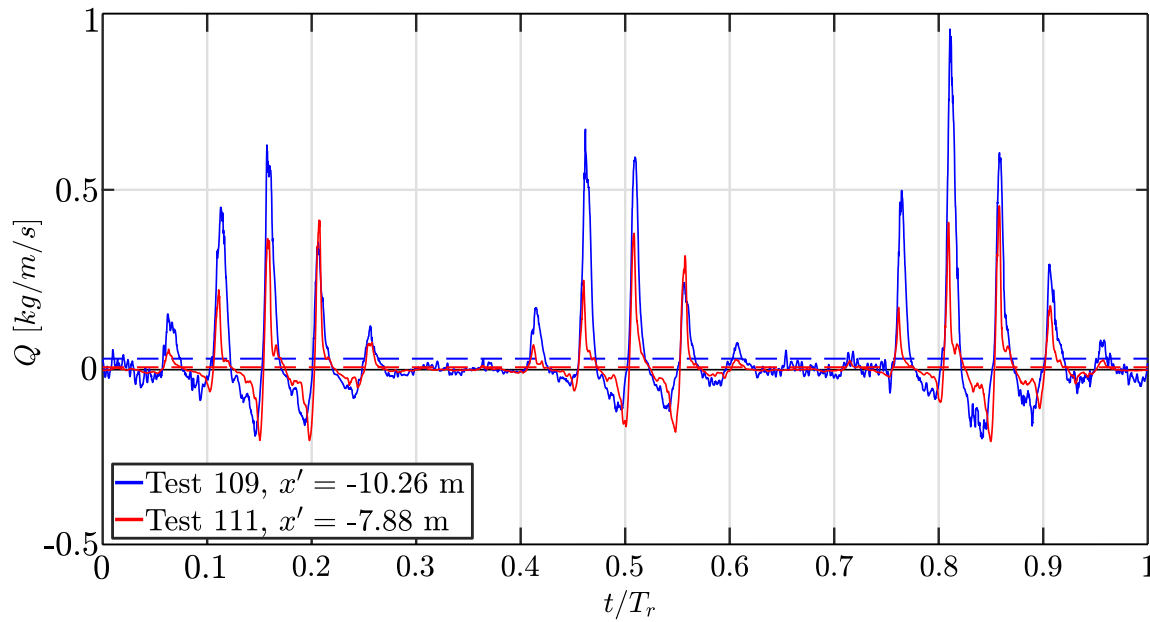


Fig. 4. Depth-integrated, time-dependent sediment flux (solid lines) measured by ACVP in positions offshore (blue) and onshore (red) of the outer bar. Horizontal dashed lines represent time-averaged net transport. Positive values indicate towards the beach and negative values away from the beach.

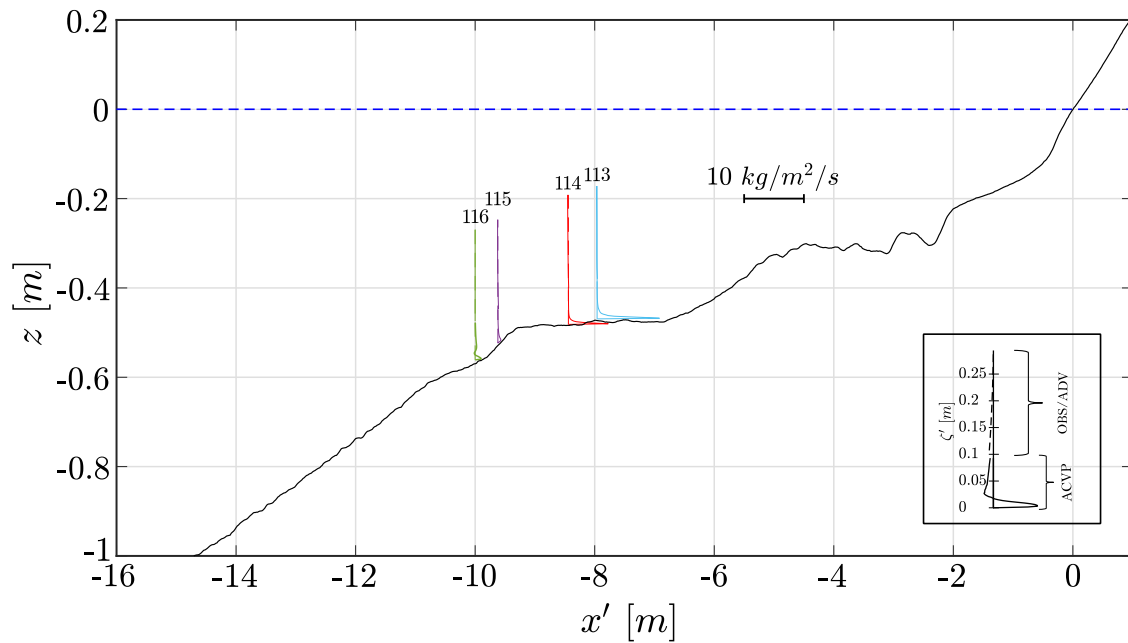


Fig. 5. Depth-resolving, time-averaged sediment flux profiles from ACVP and OBS/ADV shown in their respective relative cross-shore positions with mini-axes according to sketch in the bottom right corner and scale as shown at $x' = -5$ m. The dashed blue line represents SWL and the beach profile (solid black line) was averaged over the shown tests to improve visibility of the fluxes.

3.4.3. Berm accretion

This is reaffirmed by a plot of time-dependent berm volume (Fig. 7), integrated horizontally from the moving shoreline to a fixed reference point ($x = 80.5$ m; no morphological evolution onshorewards). Initially ($t \leq 4$ h), berm accretion is slow while the outer bar trough is being filled (Fig. 2a). Once the trough has been filled, berm accretion accelerates (Fig. 7, $5 \leq t \leq 7$ h). The phase of breaker bar re-organization (Fig. 2b) is consistent with lower berm accretion (Fig. 7, $8 \leq t \leq 10$ h). As the main breakpoint moves closer to the shoreline (Fig. 3c), another phase of berm accretion occurs (Fig. 7, $11 \leq t \leq 19$ h).

Note the differences between the two phases ($5 \leq t \leq 7$ h; $11 \leq t \leq 19$ h) of berm accretion. While the first phase (Fig. 2a)

is characterized by the initial formation of a berm with considerable vertical accretion, the second phase (Fig. 2c) focuses on accretion of the back berm (berm overwash). Interestingly, the second phase requires 8 h of wave condition A3 to accrete a similar berm volume as the first phase accreted in 4 h.

Fig. 8 provides additional detail on the underlying sediment transport processes. It shows the wave height (a) of the short waves, and suspended sediment concentration (b) in the inner surf and swash zone. Note that the analysis focuses on short waves because they dominated swash zone processes in the present experiments, see also Alsina et al. (2018) who observed short wave-dominated swash zone processes at large T_g . The figure compares a test representative of the first phase

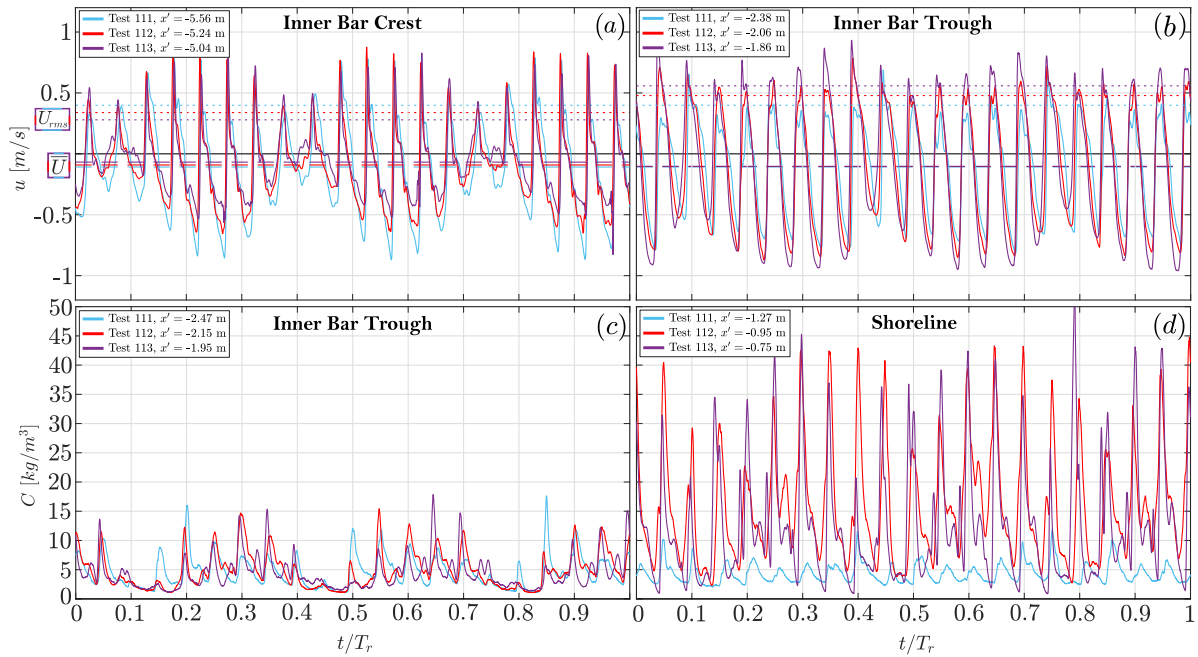


Fig. 6. Flow velocities (a, b) and suspended sediment concentrations (c, d) in positions offshore (a) and onshore (b, c, d) of the inner bar. Different colors refer to different tests: blue, red and purple in temporal order. The dashed and dotted lines (a, b) show the time-averages and root-mean-square velocities.

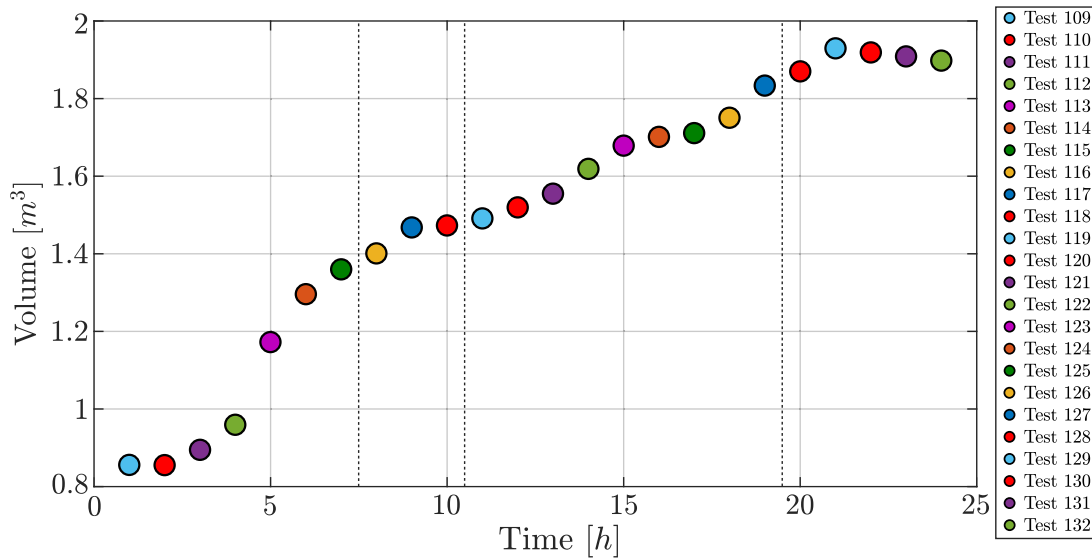


Fig. 7. Emerged volume of the berm in each test calculated by horizontal integration of the measured beach profile from the test-dependent shoreline (intersection of profile and SWL) up to a reference point at $x = 80.5$ m where no considerable morphological evolution occurs anymore. Vertical lines indicating separation into morphological phases.

of berm accretion (test 114; light blue lines) to a test representative of the second phase (test 123, red lines) — with slight differences in the sensor locations arising from profile evolution in combination with a non-moving sensor array.

In the inner surf zone ($x' \leq 0$ m), Fig. 8a shows similar short wave height in both phases of berm accretion (note the de-shoaling in the inner bar trough and the renewed shoaling of unbroken waves further onshore). Interestingly, short waves in the second phase (test 123) retain more of their wave height as they propagate in the swash zone ($x' > 0$ m). This may be related to the slight changes in beachface slope. However, spectral analysis (not shown for brevity, see Grossmann et al. (2022) for details) of measurements in the inner surf zone also shows differences in energy content and distribution. Most likely, this is a

result of differences in energy dissipation and transfer through a later onset of wave breaking, further discussed in Section 4.

Fig. 8b (see Section 2.3 for data treatment) is consistent with the water surface elevation measurements. In the swash zone, where test 123 retained more energy, suspended sediment concentrations of test 123 (red) are larger, too. Furthermore, it shows larger suspended concentrations in the onshore ($x' \approx 0.9$ m) compared to the offshore ($x' \approx 0$ m) location. This indicates increased entrainment of sediment for onshore advection (see also Alsina et al. (2018)). Most likely, the sediment only settles out of suspension further onshore ($x' \geq 2.5$ m; no measurements available), causing accretion of the back berm (berm overwash). Test 114, in contrast, shows smaller suspended concentrations at the onshore location (compare $x' \approx 0$ m to $x' \approx 1$ m). This

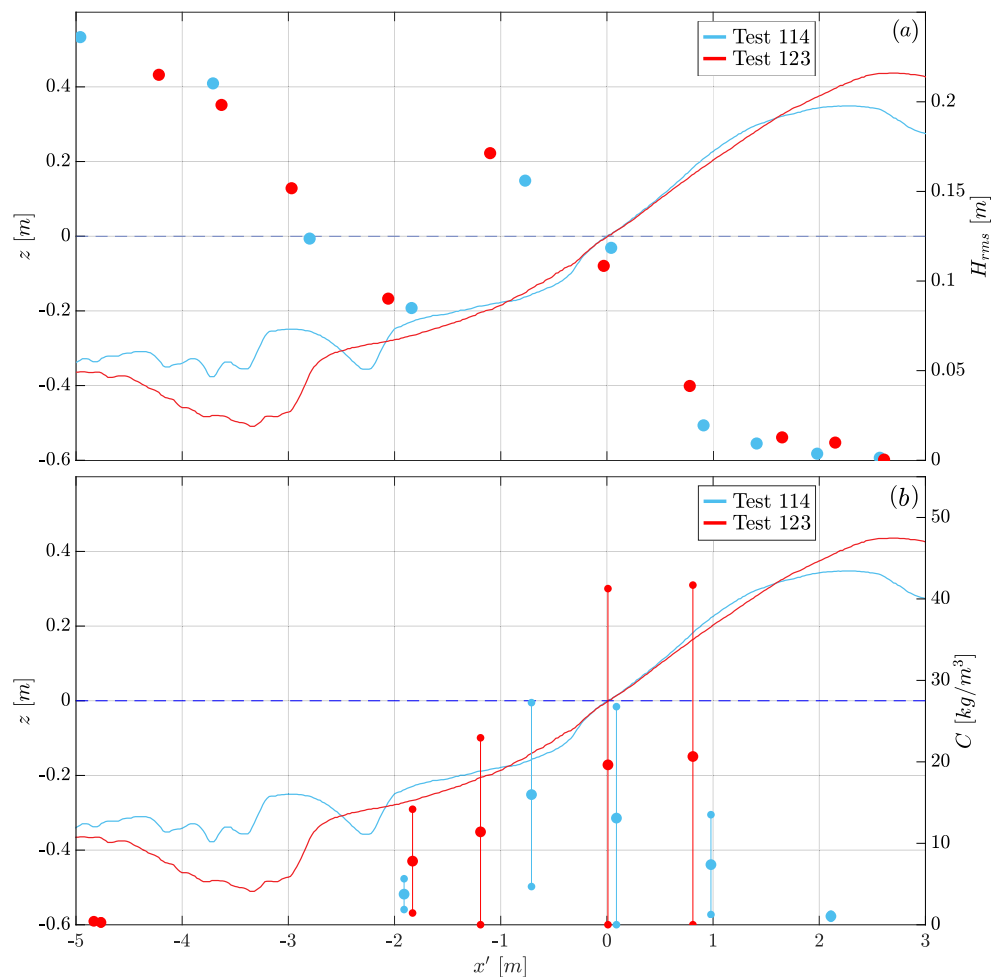


Fig. 8. Measurements (referring to right y-axis) of wave height of short waves (a) and suspended sediment concentration (b) with their beach profiles (referring to left y-axis) in a shoreline-referenced coordinate system (SWL as dark blue, dashed line). Tests representative of initial berm growth (Test 114, light blue line) and back berm growth (Test 123, red line) are shown. The concentration measurements show the time-average \pm one standard deviation.

indicates that advected sediment is already settling out of suspension, leading to deposition and berm (beachface) accretion (see also Fig. 2).

4. Discussion

4.1. Linking bar and berm morphology

This study conducted large-scale wave flume experiments of cross-shore beach profile evolution. They started from a dissipative beach profile with outer and inner bars that had been generated by an energetic storm wave condition. Upon change to a low energy, accretive wave condition, the bars dissipated, the shoreline recovered, and a berm accreted — resulting in a reflective beach profile. Measurements of hydrodynamic quantities like water surface elevation and current velocity as well as sediment concentration and transport provided details on the morphological evolution. The experiments showed that bar morphology has important links to shoreline recovery and berm accretion.

One such link is the surf-swash exchange of sediment. The present study observed bar dissipation as the shoreline and the berm accreted. The cross-shore sediment transport gradients (Fig. 2) imply that the sediment for the accretion in fact originated from the bars and the shallow inner surf zone surrounding them. This is consistent with results from other laboratory (Ruessink et al., 2016) and field (Ruiz

de Alegría-Arzaburu and Vidal-Ruiz, 2018) experiments. The exchange of sediment between bar and berm was incorporated in numerical modeling by Larson et al. (2016). They modeled changes to the berm volume as a direct consequence of changes to the bar volume. Note, however, that sediment exchange between bar and berm depends on the prevalence of processes transporting the sediment.

In this context, bar morphology also influences hydrodynamics and transport processes (feedback loop). The initial breakpoint at the start of the present experiments originated from the combination of new hydrodynamics (change from E2 to A3, Table 1) with a pre-existing (E2) quasi-equilibrium beach profile. This generated sediment transport gradients that dissipated the bars (Fig. 2a). As a result, hydrodynamic conditions changed and the breakpoint shifted onshore. This affected the transfer and dissipation of wave energy across the beach profile, generating new transport gradients. Consequently, surf-swash exchange of sediment and morphological evolution were affected (Fig. 2b/c; Section 3.2).

Other experiments in RESIST (wave condition A1) also showed an influence of initial bar morphology on hydrodynamics (wave breaking), and on the subsequent bar and berm morphology. When waves were breaking close to the outer bar, the bar was maintained during on-shore migration (AN morphology in Grossmann et al. (2023b)). Under the same wave condition (height), but starting from a different post-storm profile, breaking shifted onshore so that the outer bar dissipated

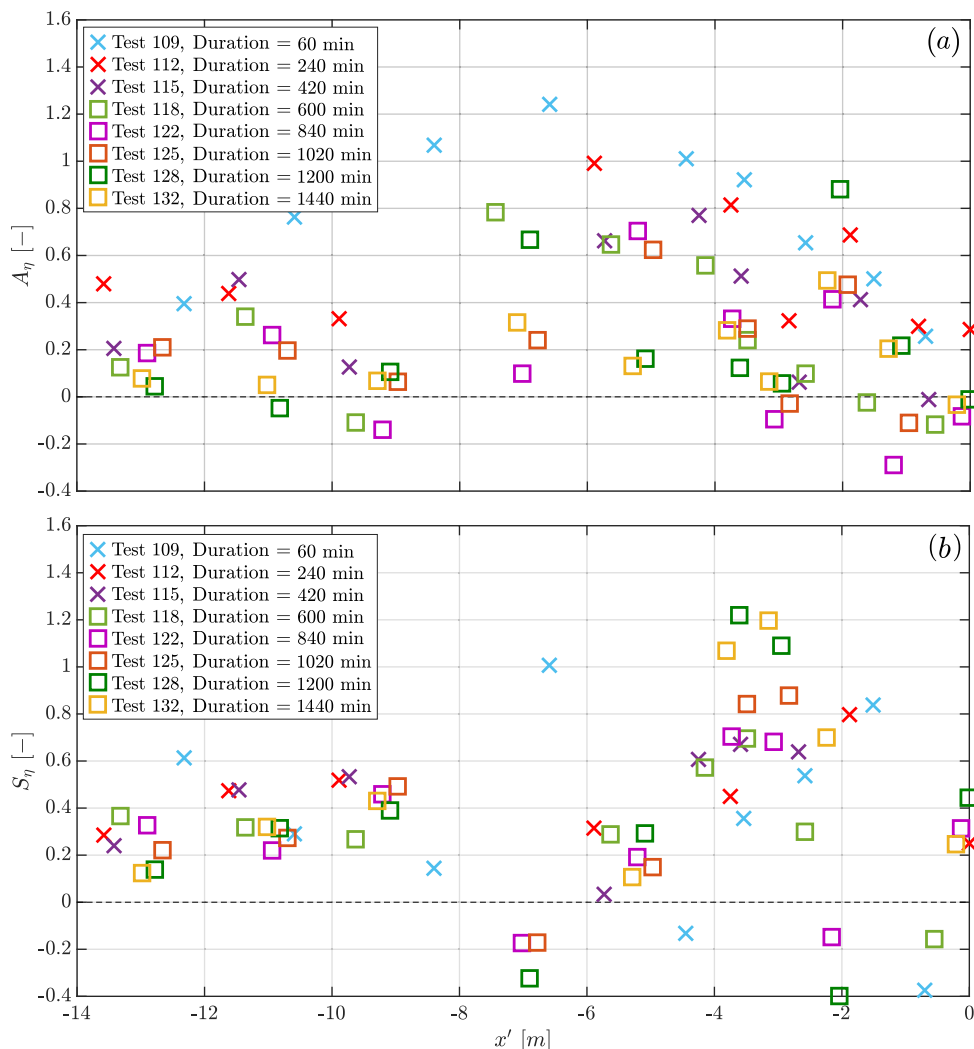


Fig. 9. Wave asymmetry (a) and skewness (b) in various tests (multiple colors), shown in shoreline-referenced cross-shore positions. Note that tests at the beginning of the accretive sequence (crosses) use different symbols than the tests towards the end of the sequence (squares). Values calculated as explained in accompanying text.

and merged with the inner bar during onshore migration (AM morphology in Grossmann et al. (2023b)). Note that the present wave condition A3 features less energy than A1 in Grossmann et al. (2023b) but the accretive sequence started from a very similar E2 post-storm profile (which led to bar maintenance, AN morphology, under A1). And there may be a tendency that larger reduction in wave height (dimensionless fall velocity) is more likely to lead to bar dissipation during onshore migration (Eichentopf et al., 2018). However, this is not simply a function of the reduction in wave height itself but rather of the resulting interactions between hydrodynamics and beach profile — including depth-induced wave breaking (and large reductions in dimensionless fall velocity may be a proxy for an onshore-shifting breakpoint). In the end, such interactions and the breaking generate the sediment transport processes, including asymmetry-related bedload and wave-breaking related suspended load, that cause morphological evolution.

4.2. Surf zone transport processes

Sediment transport processes in the surf zone will now be analyzed by discussing wave asymmetries and undertow velocity in the context

of the previous results. Wave skewness, the asymmetry about the horizontal axis, was calculated according to

$$S_{\eta} = \frac{\overline{\eta(t)^3}}{\sigma_{\eta}^3} \quad (1)$$

where the overbar in Eq. (1) represents time-averaging and σ is the standard deviation. To calculate asymmetry about the vertical axis, so-called “asymmetry”, η in the previous equation was replaced with its Hilbert transform (Elgar, 1987). Note that asymmetries arise as sinusoidal deep water waves interact with shallow bottoms, transferring energy from incident frequency bands (Phillips, 1960). Fig. 9 shows asymmetry (a) and skewness (b) from water surface elevation measurements in shoreline-referenced coordinates. Various colors indicate different tests, while different markers were used for the initial tests with offshore breaking (crosses) and subsequent tests where breaking shifted onshore (squares).

The figure shows a reduction of asymmetry (a) during the accretive sequence. Initially, the maximum occurred at the outer bar but it subsequently shifts onshore (compare light blue and red crosses to orange and yellow squares). Furthermore, wave skewness (b) takes larger values in the inner surf zone ($-4 \leq x' \leq -2$ m) towards the end of the accretive sequence.

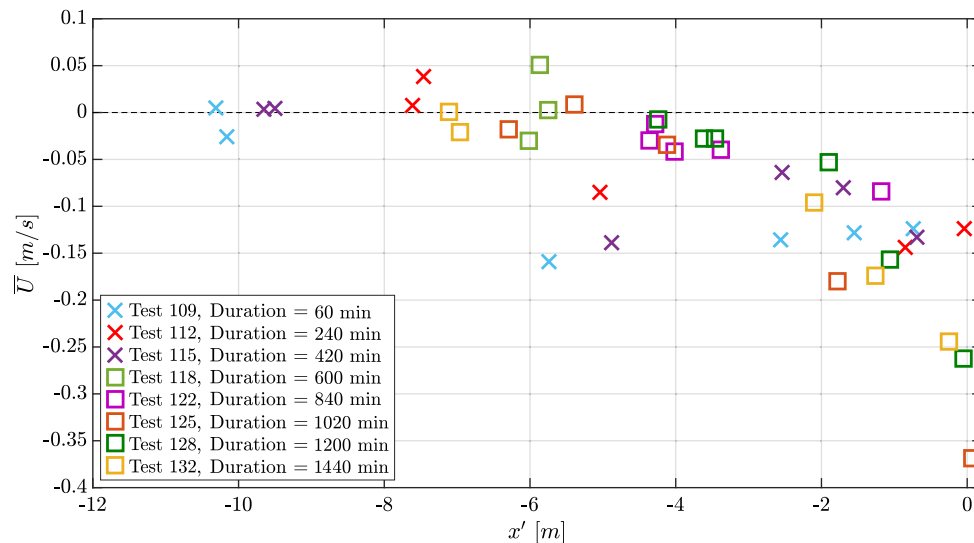


Fig. 10. Time-averaged outer flow velocities in various tests (multiple colors), shown in shoreline-referenced cross-shore positions. Note that tests at the beginning of the accretive sequence (crosses) use different symbols than the tests towards the end of the sequence (squares).

In regards to sediment transport, this indicates potential for short wave asymmetry-related bedload net onshore transport (e.g., [Dibajnia and Watanabe \(1992\)](#), [van der A et al. \(2010\)](#), [Mieras et al. \(2019\)](#) and [Grossmann et al. \(2023b\)](#)) throughout the active beach profile. As asymmetry reduces over time, the amount of short wave asymmetry-related bedload net onshore transport most likely reduces, too (see [van der A et al. \(2010\)](#), for example). Furthermore, as the maxima of asymmetry and skewness shift onshore, the maxima of short wave asymmetry-related bedload net onshore transport most likely shift onshore, too (see also [Elgar et al. \(2001\)](#)). This particularly applies to bedload-dominated transport of medium to coarse sand (e.g., [van der A et al. \(2013\)](#)) such as the present one.

The observed asymmetries partly result from wave breaking. As breaking shifts onshore, it occurs more violently and wave energy is dissipated over a narrower extent of the beach profile (and partially reflected; see also [Wright and Short \(1984\)](#)). As a result, asymmetries were larger in the beginning of the accretive sequence. There, wave energy dissipation over a larger extent of the profile left more room for gradual energy transfers during wave propagation over shallow water depth ([Padilla and Alsina \(2017\)](#)); observe also the depth increase of the surf zone in [Fig. 1](#). Note that, in agreement with the present results, field experiments (e.g., [Phillips et al. \(2017\)](#)) have also associated beach recovery with gradual onshore migration of the breakpoint.

[Fig. 10](#) shows time-averaged velocity measurements at shoreline-referenced coordinates in different tests (various colors). Again, cross markers indicate tests with offshore breaking and square markers tests where breaking shifted onshore. Note that undertow originates from wave breaking to compensate for onshore mass flux and energy dissipation (e.g., [Svendsen \(1984\)](#)). Consistent with observations of wave breaking (Section 3.3), the initial maxima of undertow ($-6 \leq x' \leq -4$ m) shift onshore. In fact, towards the end of the accretive sequence, undertow is low throughout most of the active beach profile and only increases very close to the shoreline ($x' \geq -2$ m).

In regards to sediment transport, this indicates potential for suspended net offshore transport (e.g., [Gallagher et al. \(1998\)](#) and [Grossmann et al. \(2022\)](#)) between the outer and inner bar in the initial tests. Such transport occurs because the offshore-directed current entrains sediment from the bed and transports suspended sediments (also the ones entrained by short waves). As wave breaking and undertow shift onshore, the profile region over which suspended net offshore transport is active shifts onshore, too.

In combination with the previous observations of wave asymmetry, this explains the sediment transport measurements that led to outer bar dissipation (Section 3.4.1). Initially, the bar trough is filled through the net offshore transport contributions from undertow and considerable net onshore transport under large wave asymmetry. As undertow shifts onshore ([Fig. 10](#)), asymmetry decreases and shifts onshore, too ([Fig. 9](#)) — but it remains high enough to cause continued erosion of the outer bar region in the absence of suspended net offshore transport ([Fig. 5](#)).

4.3. Swash zone transport processes

The field experiments of [Weir et al. \(2006\)](#) are one of the few studies that investigated berm accretion in detail. The rapid horizontal and vertical accretion observed in the first morphological phase of the present experiments ([Fig. 1](#), $t \leq 420$ min and [Fig. 2a](#)) is similar to their berm accretion mode 1. Note that [Weir et al. \(2006\)](#) identified berm overwash as a key process of berm accretion. Overwash is also evident in the third morphological phase of the present experiments ([Fig. 2c](#)), where berm accretion mainly occurred on the landward side of the berm and short wave bores propagated deep into the swash zone (Section 3.4.3).

In regards to the controls of berm overwash, [Weir et al. \(2006\)](#) and [Jensen et al. \(2009\)](#) note the importance of rising tides, effectively allowing waves to penetrate deeper into the swash zone to overwash the berm. The present laboratory experiments did not include any water level fluctuations similar to tides. Thus, in the present experiments, the amount and frequency distribution of wave energy reaching the swash zone, and the waves' interaction with the beachface, control swash overtopping.

In this context, the onshore shift of the breakpoint (Section 3.3) is of central importance. Initially ([Fig. 3a](#)), less energy reaches the swash zone because wave energy is dissipated over a large cross-shore extent (Section 3.4.3). The berm accretes nevertheless ([Fig. 7](#), $t \leq 7$ h), because the berm height is much lower than a typical berm height under the present wave condition (disequilibrium between beach profile and hydrodynamics after the change from energetic to low energy waves). This is also referenced by [Weir et al. \(2006\)](#) as the reason for their initial berm accretion in mode 1.

Subsequently ([Fig. 3b](#)), the beachface has steepened ($0 \leq x' \leq 2.5$ m) while wave energy is still dissipated over a considerable extent of the beach profile (breaking around $x' \approx -4.5$ m). As a result, relatively little

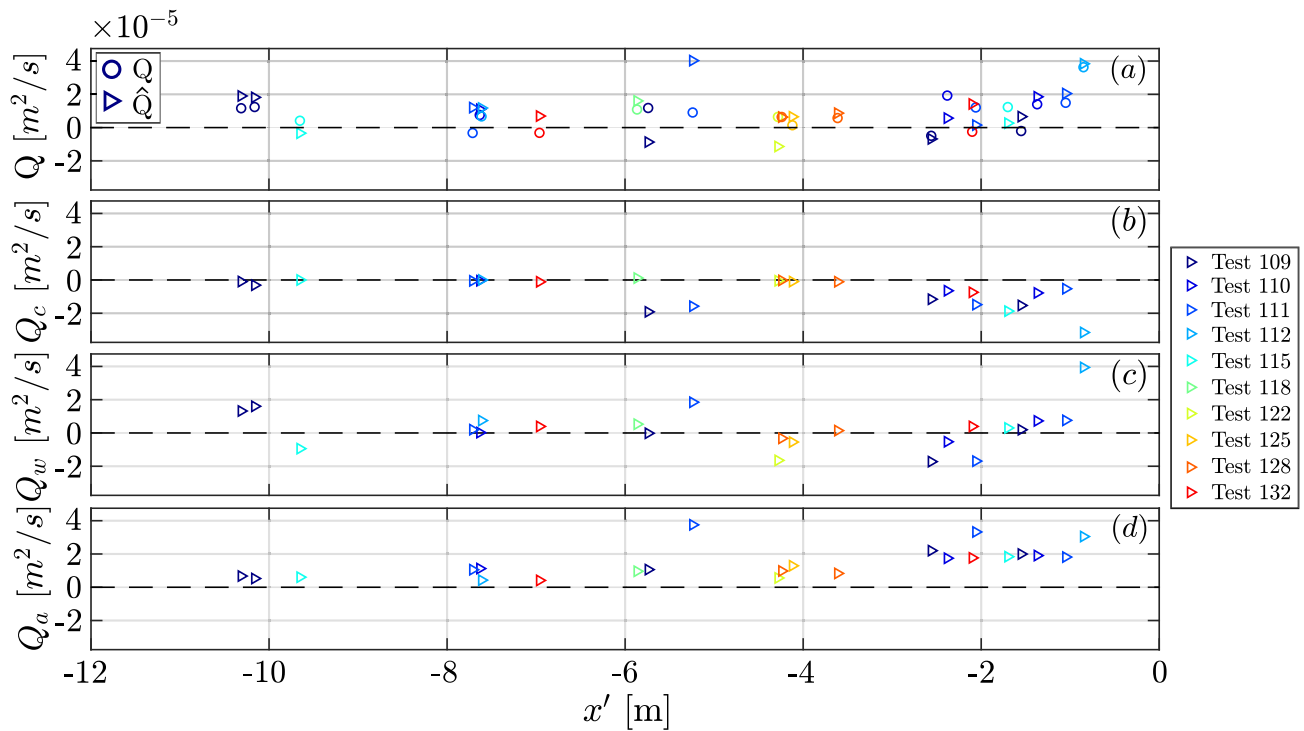


Fig. 11. Comparison of measured (Q) and estimated (\hat{Q}) transport (a; mini-legend) with contributions from current-related transport (b), wave(skewness)-related transport (c), and wave asymmetry-related transport (d). Results in different tests over the accretive sequence (legend on the right) are shown in shoreline-referenced cross-shore positions.

wave energy reaches the swash zone while downslope transport from steepening (see [Masselink and Puleo \(2006\)](#), for example) increases so that berm accretion slows down (Fig. 7, $8 \leq t \leq 10$ h). Once breaking shifts further onshore (Fig. 3c), more wave energy reaches the swash zone (Fig. 8a) to increase berm overwash and accretion again (Fig. 7, $11 \leq t \leq 19$ h; Section 3.4.3). Through further steepening of the beachface (Fig. 1, $t \geq 1020$ min), the profile reaches quasi-equilibrium with the hydrodynamics (Fig. 2d).

4.4. Sediment transport estimation

Measurements of flow velocity were used to estimate net sediment transport (\hat{Q}) and compare with transport measurements (Q) from a mass balance (Section 2.3). Due to their success under similar morphological conditions in the field, the formulations of [Hoefel and Elgar \(2003\)](#) and [Hsu et al. \(2006\)](#) were chosen, so that:

$$\hat{Q} = Q_c + Q_w + Q_a \quad (2)$$

where Q_c is the current-related transport (second term of Equation 13 in [Hsu et al. \(2006\)](#)), Q_w is the wave(skewness)-related transport (first term of Equation 13 in [Hsu et al. \(2006\)](#)), and Q_a is the asymmetry-related transport (Equation 1 in [Hoefel and Elgar \(2003\)](#)). Furthermore, the same parameter settings as [Hsu et al. \(2006\)](#) were applied, apart from the settling velocity measured in the present experimental setup (Section 2.1).

Note that the output of such Energetics-type models ([Bailard, 1981](#)) is heavily dependent on calibration factors ([Dubarbier et al., 2015](#)). Based on data analysis in the present contribution, showing little sediment suspension, the wave-related calibration factor ($C_w = 0.045$) was set to 1.5 times the current-related factor ($C_c = 0.03$). Furthermore, the critical acceleration was set to the same value ($a_{crit} = 0.2$) as suggested by [Hoefel and Elgar \(2003\)](#) and the calibration factor was slightly adjusted to a value ($K_a = 0.188 \cdot 10^{-4}$) used by [Dubarbier et al. \(2015\)](#). Velocity measurements were subjected to an additional quality

Table 2

Root-mean-squared error (RMSE) between measured and estimated net transport in tests 109, 110, 111, 112, 115, 118, 122, 125, 128, 132.

Considered terms	RMSE [m^2/s]
$Q_c + Q_w + Q_a$	$1.16 \cdot 10^{-5}$
$Q_c + Q_a$	$1.18 \cdot 10^{-5}$
$Q_c + Q_w$	$1.82 \cdot 10^{-5}$

control for reasonable representation of wave shapes and accelerations, time series were only accepted if less than 1% of data were missing from T_r (to avoid bias in net transport estimation), and fuzzy measurements were smoothed with a moving average filter of less than 1 s. Note that the transport estimations were compared to the transport measurement at the closest cross-shore location (always within 2 cm) within the same respective test (dashed lines in Fig. 2).

Fig. 11 shows the estimated sediment transport from the outer bar through the inner surf zone during various tests over the accretive sequence (same tests as shown in Figs. 9 and 10 but adding tests 110 and 111 for more detail in the beginning). In Fig. 11a it becomes visible that onshore transport was replicated in general but, at times, there was over- and underestimation. Considering the difficulty in estimating low magnitude net onshore transport with a practically-applicable, engineering-type model, the agreement (first row of Table 2) is reasonably good (RMSE amounting to 32% of the largest transport measured). Figs. 11b/c/d show estimated transport contributions from single components to provide additional detail on the sediment transport processes discussed previously.

The current-related transport (Fig. 11b) is low in most cross-shore locations, consistent with undertow shown in Fig. 10. The maximum initially observed at the outer bar ($-6 \leq x' \leq 5$ m), which contributes to outer bar dissipation (Section 3.4.1), decreases in subsequent tests (compare blue to green markers). This is consistent with the onshore shift of suspended net offshore transport explained previously (Section 4.2). As a result, subsequent tests feature larger magnitudes in the

inner surf zone ($x' \geq -3$ m; compare light blue to dark blue markers). The wave(skewness)-related transport (Fig. 11c) shows net onshore but also net offshore contributions. The latter are unexpected from physical considerations of the present grain size (e.g., van der A et al. (2013)) and result from large troughs in the input velocity signals. Initially, asymmetry-related net onshore transport (Fig. 11d; $-8 \leq x' \leq -6.5$ m) contributes to filling the outer bar trough. As asymmetry decreases in subsequent tests (Fig. 9), the estimated net onshore transport decreases, too (compare dark blue to light blue and red markers). Nevertheless, it still provides a noticeable net onshore contribution which causes the continued erosion of the outer bar (Section 3.4.1) in the absence of suspended net offshore transport (see also Grossmann et al. (2023b)). Throughout the accretive sequence, wave asymmetry contributes net onshore transport over the inner surf zone, feeding berm growth ($x' \geq -3$ m).

Overall, considering $\hat{Q} = Q_c + Q_w + Q_a$ only performs slightly better than $\hat{Q} = Q_c + Q_a$ but considerably better than $\hat{Q} = Q_c + Q_w$ (Table 2). In the present context, the asymmetry-related transport seems a more reliable predictor of the net onshore-directed bedload which this study and others (Mieras et al., 2019; Grossmann et al., 2023b) observed to be crucial for bar onshore migration and beach recovery. Nevertheless, the present agreement between transport measurements and estimation is still crude, heavily dependent on calibration (which often cannot be known beforehand), and a more detailed assessment of bedload would be necessary — for example considering intergranular forces (e.g., Revil-Baudard and Chauchat (2013)).

5. Conclusions

This paper conducted large-scale wave flume experiments to study beach recovery after storms. To generate the initial beach profile, high energy storm waves were applied until morphological evolution became negligibly low. Subsequently, a very low energy, accretive wave condition was applied for long experimental duration (24 h) until morphological evolution became negligibly low. Sediment transport (including bedload) was measured and associated to observations of hydrodynamic forcing, including energetics-based transport formulations. This allowed to observe, at unprecedented detail, the morphological evolution from a fully dissipative to a fully reflective beach state. The results lead to the following conclusions:

- Morphological evolution occurred in four phases with distinct patterns of cross-shore transport gradients, surf-swash sand exchange, and berm accretion.
- A breakpoint shift from bars to shoreline controlled beach recovery. The shift enabled berm overwash in the swash zone to complete the transition to a fully-reflective beach profile.
- Bedload net onshore transport under wave crests (associated with short wave asymmetry) controlled sediment transport gradients in the surf zone. Undertow and sediment suspension were generally low and only had limited influence on morphological evolution.

These conclusions provide novel insight into the complex, and poorly investigated, phenomenon of beach recovery and berm accretion, which is an integral aspect of seasonal beach profile evolution. To support additional physical analyses and numerical model development, the presented data will be made accessible by the authors upon request.

CRedit authorship contribution statement

Florian Grossmann: Writing – review & editing, Writing – original draft, Visualization, Validation, Supervision, Software, Resources, Project administration, Methodology, Investigation, Funding acquisition, Formal analysis, Data curation, Conceptualization. **David Hurther:** Writing – review & editing, Supervision, Software, Methodology,

Formal analysis, Conceptualization. **Agustín Sánchez-Arcilla:** Writing – review & editing, Supervision, Project administration, Investigation, Funding acquisition, Conceptualization. **Enrique M. Padilla:** Writing – review & editing, Software, Formal analysis. **José M. Alsina:** Writing – review & editing, Writing – original draft, Visualization, Supervision, Software, Resources, Project administration, Methodology, Investigation, Funding acquisition, Formal analysis, Conceptualization.

Declaration of competing interest

The authors declare that they have no known competing financial interests or personal relationships that could have appeared to influence the work reported in this paper.

Data availability

Data will be made available on request.

Acknowledgments

We thank two anonymous reviewers for their valuable comments which helped to improve the manuscript. We acknowledge funding from the REST-COAST project which receives funding from the EU Horizon 2020 Research and Innovation Programme under Grant Agreement number 101037097. JA acknowledges funding from the Serra Hünter Programme (SHP). We thank Joaquim Sospedra, Oscar Galego, Dr. Andrea Marzeddu, Dr. Iván Cáceres, and Dr. Joep van der Zanden for their contributions to the experiments.

Appendix. Analysis of the wave generation

The energy content at the low frequencies is fundamentally explained by the energy content at the group frequency f_g , i.e., the energy content at the repetition frequency f_r is orders of magnitude lower. Fig. A.12 illustrates the separation of the existing long wave trains at the group frequency f_g . Fig. A.12a shows the cross-shore wave amplitude (A) at f_g where one and only one well defined node-antinode pattern exists (see the undulating pattern). Based on this single pattern, Padilla and Alsina (2022) (Eq. (5)) indicates that only two wave trains propagate within f_g (one Ingoing Bound Wave and one Outgoing Free Wave) with no spurious energy content belonging to any unwanted wave train generated. This assumption is confirmed by the outcomes of the wave separation. These outcomes are displayed in Fig. A.12a.

The separated (Sep) cross-shore amplitudes for the Ingoing Bound Wave (IBW) and Outgoing Free Wave (OFW) are in good agreement with their theoretical (Th) cross-shore growth. The theoretical evolution for the free wave (OFW) is based on linear shoaling, whereas the evolution of the bound waves is $A^{IBW} \propto h^{-\alpha}$, as observed by Battjes et al. (2004) and van Dongeren et al. (2007). A negligible residual energy content (around 4% of the energy content of IBW) not being explained by the IBW or the OFW is displayed (green dots). Based on the phases of the separated IBW and OFW, the estimation of the nodes (red arrow) and antinodes (black arrow) given by Padilla and Alsina (2020) (Eqs. (13–14)) explains the locations of the observed node-antinode pattern. The undulation due the pair [IBW, OFW] is also clear in the space-time contour in Fig. A.12b. The dominant trajectory of the surface elevation at f_g (η_{f_g}) follows the time-space trajectory of the IBW (black solid line). Therefore, the IBW dominates over the OFW (as expected).

In summary, the wave condition A3, as shown here in Test 125, presents a very low level of free-wave contamination (negligible residual energy content). This conclusion, derived from the wave separation proposed by Padilla and Alsina (2020), is valid as the separation method is valid seaward of the surf zone. Within the surf zone onshorewards, the actual figures of the IBW and OFW must be carefully considered, but are not in conflict with the clear conclusion of negligible free-wave contamination.

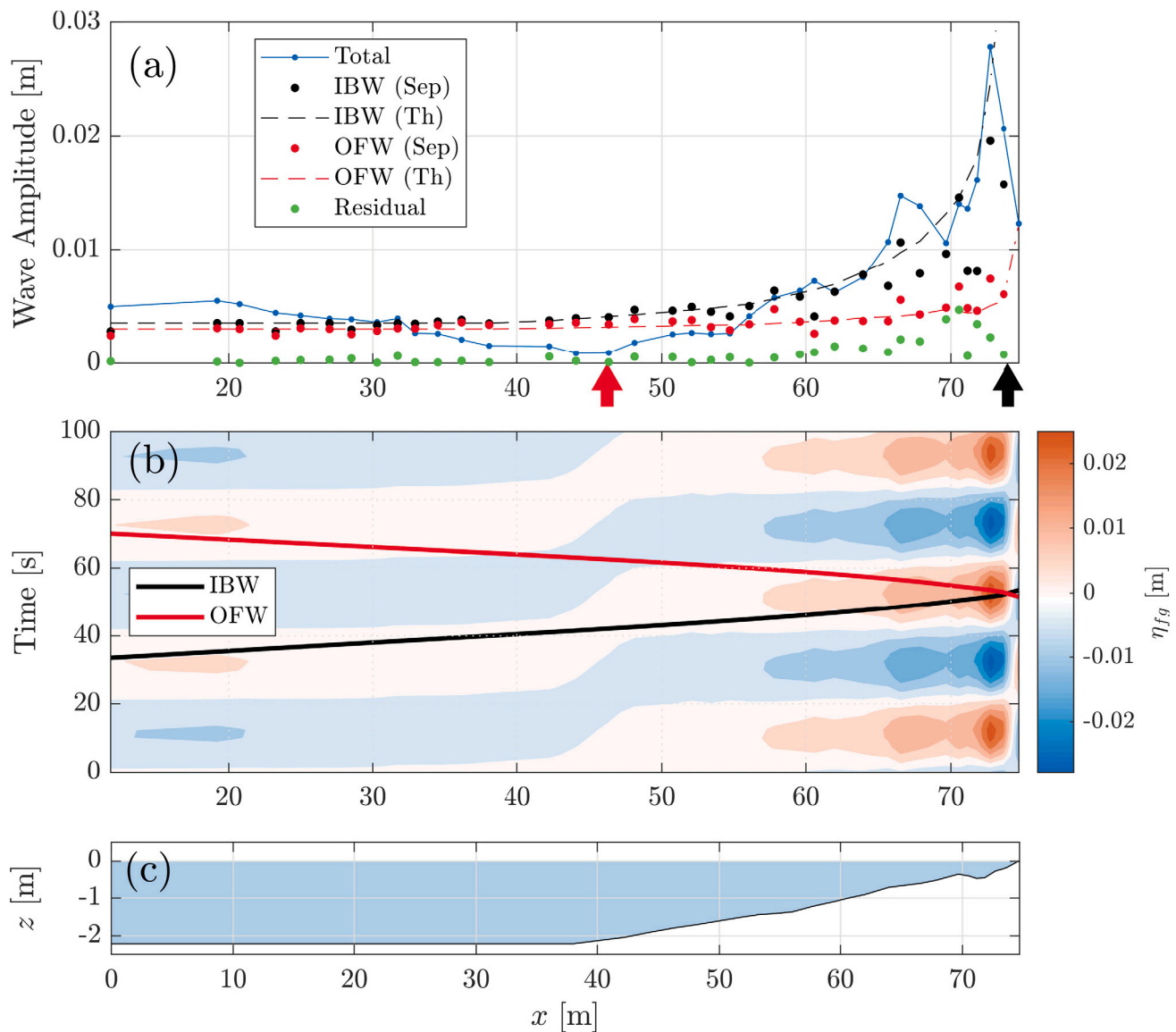


Fig. A.12. Wave generation in test 125. Plot (a) shows the cross-shore evolution of the total wave amplitude at f_g alongside the theoretical (Th) and separated (Sep) wave amplitudes of IBW (black) and OFW (red). A negligible residual energy content not being explained by the IBW or the OFW is displayed in green. The red and black arrows are the set of computed locations of the antinodes belonging to the pair [IBW, OFW]. Plot (b) shows the η_{fg} contour plot where the time-space trajectories of IBW (black) and OFW (red) are displayed. Plot (c) illustrates the corresponding water depth.

References

Alsina, J.M., Cáceres, I., Brocchini, M., Baldock, T.E., 2012. An experimental study on sediment transport and bed evolution under different swash zone morphological conditions. *Coast. Eng.* 68, 31–43. <http://dx.doi.org/10.1016/j.coastaleng.2012.04.008>.

Alsina, J.M., van der Zanden, J., Cáceres, I., Ribberink, J.S., 2018. The influence of wave groups and wave-swash interactions on sediment transport and bed evolution in the swash zone. *Coast. Eng.* 140, 23–42. <http://dx.doi.org/10.1016/j.coastaleng.2018.06.005>.

Bailard, J.A., 1981. An energetics total load sediment transport model for a plane sloping beach. *J. Geophys. Res.: Oceans* 86 (C11), 10938–10954. <http://dx.doi.org/10.1029/JC086iC11p10938>.

Baldock, T.E., Alsina, J.M., Cáceres, I., Vicinanza, D., Contestabile, P., Power, H., Sánchez-Arcilla, A., 2011. Large-scale experiments on beach profile evolution and surf and swash zone sediment transport induced by long waves, wave groups and random waves. *Coast. Eng.* 58, <http://dx.doi.org/10.1016/j.coastaleng.2010.10.006>.

Baldock, T.E., Hughes, M.G., Day, K., Louys, J., 2005. Swash overtopping and sediment overwash on a truncated beach. *Coast. Eng.* 52, 633–645. <http://dx.doi.org/10.1016/j.coastaleng.2005.04.002>.

Battjes, J.A., Bakkenes, H.J., Janssen, T.T., van Dongeren, A.R., 2004. Shoaling of subharmonic gravity waves. *J. Geophys. Res.: Oceans* 109 (C2), <http://dx.doi.org/10.1029/2003JC001863>.

Bonneton, P., Lannes, D., Martins, K., Michallet, H., 2018. A nonlinear weakly dispersive method for recovering the elevation of irrotational surface waves from pressure measurements. *Coast. Eng.* 138, 1–8. <http://dx.doi.org/10.1016/j.coastaleng.2018.04.005>.

Dibajnia, M., Watanabe, A., 1992. Sheet flow under nonlinear waves and currents. *Coast. Eng. Proc.* 1 (23), <http://dx.doi.org/10.1061/9780872629332.154>.

Dubarbier, B., Castelle, B., Marieu, V., Ruessink, B.G., 2015. Process-based modeling of cross-shore sandbar behavior. *Coast. Eng.* 95, 35–50. <http://dx.doi.org/10.1016/j.coastaleng.2014.09.004>.

Eichentopf, S., Alsina, J.M., Christou, M., Kuriyama, Y., Karunarathna, H., 2020b. Storm sequencing and beach profile variability at Hasaki, Japan. *Mar. Geol.* 424, 106153. <http://dx.doi.org/10.1016/j.margeo.2020.106153>.

Eichentopf, S., Cáceres, I., Alsina, J.M., 2018. Breaker bar morphodynamics under erosive and accretive wave conditions in large-scale experiments. *Coast. Eng.* 138, 36–48. <http://dx.doi.org/10.1016/j.coastaleng.2018.04.010>.

Eichentopf, S., van der Zanden, J., Cáceres, I., Baldock, T.E., Alsina, J.M., 2020a. Influence of storm sequencing on breaker bar and shoreline evolution in large-scale experiments. *Coast. Eng.* 157, <http://dx.doi.org/10.1016/j.coastaleng.2020.103659>.

Elgar, S., 1987. Relationships involving third moments and bispectra of a harmonic process. *IEEE Trans. Acoust. Speech Signal Process.* 35 (12), 1725–1726. <http://dx.doi.org/10.1109/TASSP.1987.1165090>.

- Elgar, S., Gallagher, E.L., Guza, R.T., 2001. Nearshore sandbar migration. *J. Geophys. Res.*: Oceans 106, 11623–11627. <http://dx.doi.org/10.1029/2000JC000389>.
- Flick, R.E., Guza, R.T., 1980. Paddle generated waves in laboratory channels. *J. Waterw. Port Coast. Ocean Div.* 106 (1), 79–97. <http://dx.doi.org/10.1061/JWPDCD.0000193>, 106 (WW1).
- Fromant, G., Mieras, R.S., Revil-Baudard, T., Puleo, J.A., Hurther, D., Chauchat, J., 2018. On bedload and suspended load measurement performances in sheet flows using acoustic and conductivity profilers. *J. Geophys. Res.*: Earth Surf. 123 (10), 2546–2562. <http://dx.doi.org/10.1029/2017JF004560>.
- Gallagher, E.L., Elgar, S., Guza, R.T., 1998. Observations of sand bar evolution on a natural beach. *J. Geophys. Res.*: Oceans 103 (C2), 3203–3215. <http://dx.doi.org/10.1029/97JC02765>.
- Grossmann, F., Hurther, D., Sánchez-Arcilla, A., Alsina, J.M., 2023b. Influence of the initial beach profile on the sediment transport processes during post-storm onshore bar migration. *J. Geophys. Res.*: Oceans 128, e2022JC019299. <http://dx.doi.org/10.1029/2022JC019299>.
- Grossmann, F., Hurther, D., van der Zanden, J., Cáceres, I., Sánchez-Arcilla, A., Alsina, J.M., 2022. Near-bed sediment transport during offshore bar migration in large-scale experiments. *J. Geophys. Res.*: Oceans 127, e2021JC017756. <http://dx.doi.org/10.1029/2021JC017756>.
- Grossmann, F., Hurther, D., van der Zanden, J., Sánchez-Arcilla, A., Alsina, J.M., 2023a. Near-bed sediment transport processes during onshore bar migration in large-scale experiments: Comparison with offshore bar migration. *J. Geophys. Res.*: Oceans 128, e2022JC018998. <http://dx.doi.org/10.1029/2022JC018998>.
- Hine, A.C., 1979. Mechanisms of berm development and resulting beach growth along a barrier spit complex. *Sedimentology* 26, 333–351. <http://dx.doi.org/10.1111/j.1365-3091.1979.tb00913.x>.
- Hoefel, F., Elgar, S., 2003. Wave-induced sediment transport and sandbar migration. *Science* 299 (5614), 1885–1887. <http://dx.doi.org/10.1126/science.1081448>.
- Hsu, T.-J., Elgar, S., Guza, R.T., 2006. Wave-induced sediment transport and onshore sandbar migration. *Coast. Eng.* 53 (10), 817–824. <http://dx.doi.org/10.1016/j.coastaleng.2006.04.003>.
- Hughes, M., Turner, I., 1999. The beach face. In: Short, A.D. (Ed.), *Handbook of Beach and Shoreface Morphodynamics*. John Wiley and Sons, Chichester, ISBN: 978-0-471-96570-1.
- Hurther, D., Thorne, P.D., Bricault, M., Lemmin, U., Barnoud, J.-M., 2011. A multi-frequency acoustic concentration and velocity profiler (ACVP) for boundary layer measurements of fine-scale flow and sediment transport processes. *Coast. Eng.* 58, <http://dx.doi.org/10.1016/j.coastaleng.2011.01.006>.
- Jensen, S.G., Aagaard, T., Baldock, T.E., Kroon, A., Hughes, M., 2009. Berm formation and dynamics on a gently sloping beach; the effect of water level and swash overtopping. *Earth Surf. Process. Landf.* 34, 1533–1546. <http://dx.doi.org/10.1002/esp.1845>.
- King, C.A.M., Williams, W.W., 1949. The formation and movement of sand bars by wave action. *Geogr. J.* 113, 70–85. <http://dx.doi.org/10.2307/1788907>.
- Larson, M., Palalane, J., Fredriksson, C., Hanson, H., 2016. Simulating cross-shore material exchange at decadal scale. Theory and model component validation. *Coast. Eng.* 116, 57–66. <http://dx.doi.org/10.1016/j.coastaleng.2016.05.009>.
- Masselink, G., Puleo, J.A., 2006. Swash-zone morphodynamics. *Cont. Shelf Res.* 26, 661–680. <http://dx.doi.org/10.1016/j.csr.2006.01.015>.
- Mieras, R.S., Puleo, J.A., Anderson, D., Hsu, T.-J., Cox, D.T., Calantoni, J., 2019. Relative contributions of bed load and suspended load to sediment transport under skewed-asymmetric waves on a sandbar crest. *J. Geophys. Res.*: Oceans 124 (2), 1294–1321. <http://dx.doi.org/10.1029/2018JC014564>.
- Padilla, E.M., Alsina, J.M., 2017. Transfer and dissipation of energy during wave group propagation on a gentle beach slope. *J. Geophys. Res.*: Oceans 122, <http://dx.doi.org/10.1002/2017JC012703>.
- Padilla, E.M., Alsina, J.M., 2020. A general framework for wave separation in the frequency domain. *Coast. Eng.* 158, 103686. <http://dx.doi.org/10.1016/j.coastaleng.2020.103686>.
- Padilla, E.M., Alsina, J.M., 2022. Assessment and improvement of the wave generation accuracy using a wave separation method. *Ocean Eng.* 250 (3), 110932. <http://dx.doi.org/10.1016/j.oceaneng.2022.110932>.
- Phillips, O., 1960. On the dynamics of unsteady gravity waves of finite amplitude part 1. The elementary interactions. *J. Fluid Mech.* 9 (2), 193–217. <http://dx.doi.org/10.1017/S0022112060001043>.
- Phillips, M.S., Harley, M.D., Turner, I.L., Splinter, K.D., Cox, R.J., 2017. Shoreline recovery on wave-dominated sandy coastlines: the role of sandbar morphodynamics and nearshore wave parameters. *Mar. Geol.* 385, 146–159. <http://dx.doi.org/10.1016/j.margeo.2017.01.005>.
- Rafati, Y., Hsu, T.J., Elgar, S., Raubenheimer, B., Quataert, E., van Dongeren, A., 2021. Modeling the hydrodynamics and morphodynamics of sandbar migration events. *Coast. Eng.* 166, 103885. <http://dx.doi.org/10.1016/j.coastaleng.2021.103885>.
- Revil-Baudard, T., Chauchat, J., 2013. A two-phase model for sheet flow regime based on dense granular flow rheology. *J. Geophys. Res.*: Oceans 118, 619–634. <http://dx.doi.org/10.1029/2012JC008306>.
- Ruessink, B.G., Blenkinsopp, C., Brinkkemper, J.A., Castelle, B., Dubarbier, B., Grasso, F., Puleo, J.A., Lanckriet, T., 2016. Sandbar and beach-face evolution on a prototype coarse sandy barrier. *Coast. Eng.* 113, 19–32. <http://dx.doi.org/10.1016/j.coastaleng.2015.11.005>.
- Ruiz de Alegría-Arزابuru, A., Vidal-Ruiz, J., 2018. Beach recovery capabilities after El Niño 2015–2016 at Ensenada Beach, Northern Baja California. *Ocean Dyn.* 68, 749–759. <http://dx.doi.org/10.1007/s10236-018-1164-6>.
- Svendsen, I.A., 1984. Mass flux and undertow in a surf zone. *Coast. Eng.* 8 (4), 347–365. [http://dx.doi.org/10.1016/0378-3839\(84\)90030-9](http://dx.doi.org/10.1016/0378-3839(84)90030-9).
- van der A, D.A., O'Donoghue, T., Ribberink, J.S., 2010. Measurements of sheet flow transport in acceleration-skewed oscillatory flow and comparison with practical formulations. *Coast. Eng.* 57 (3), 331–342. <http://dx.doi.org/10.1016/j.coastaleng.2009.11.006>.
- van der A, D.A., Ribberink, J.S., van der Werf, J.J., O'Donoghue, T., Buijsrogge, R.H., Kranenburg, W.M., 2013. Practical sand transport formula for non-breaking waves and currents. *Coast. Eng.* 76, 26–42. <http://dx.doi.org/10.1016/j.coastaleng.2013.01.007>.
- van Dongeren, A.R., Battjes, J.A., Janssen, T.T., van Noorloos, J., Steenhauer, K., Steenbergen, G., Reniers, A., 2007. Shoaling and shoreline dissipation of low-frequency waves. *J. Geophys. Res.*: Oceans 112 (C2), <http://dx.doi.org/10.1029/2006JC003701>.
- van Enckevort, I.M.J., Ruessink, G.B., 2003. Video observations of nearshore bar behaviour. Part 1: alongshore uniform variability. *Cont. Shelf Res.* 23 (5), 501–512. [http://dx.doi.org/10.1016/S0278-4343\(02\)00234-0](http://dx.doi.org/10.1016/S0278-4343(02)00234-0).
- van Rijn, L.C., Tonnon, P.K., Walstra, D.J.R., 2011. Numerical modelling of erosion and accretion of plane sloping beaches at different scales. *Coast. Eng.* 58 (7), 637–655. <http://dx.doi.org/10.1016/j.coastaleng.2011.01.009>.
- Weir, F.M., Hughes, M.G., Baldock, T.E., 2006. Beach face and berm morphodynamics fronting a coastal lagoon. *Geomorphology* 82 (1–4), 331–346. <http://dx.doi.org/10.1016/j.geomorph.2006.05.015>.
- Wijnberg, K., Kroon, A., 2002. Barred beaches. *Geomorphology* 48 (1), 103–120. [http://dx.doi.org/10.1016/S0169-555X\(02\)00177-0](http://dx.doi.org/10.1016/S0169-555X(02)00177-0).
- Winant, C.D., Inman, D.L., Nordstrom, C.E., 1975. Description of seasonal beach changes using empirical eigenfunctions. *J. Geophys. Res.* 80 (15), 1979–1986. <http://dx.doi.org/10.1029/JC080i015p01979>.
- Wright, L.D., Short, A.C., 1984. Morphodynamic variability of surf zones and beaches: A synthesis. *Mar. Geol.* 56 (1–4), 93–118. [http://dx.doi.org/10.1016/0025-3227\(84\)90008-2](http://dx.doi.org/10.1016/0025-3227(84)90008-2).